Check for updates

Size control of shape switchable micronetworks by fast two-step microfluidic templating

Fabian Friess[1,2], Andreas Lendlein[1,2,a)] (iD), Christian Wischke[1,3,a)] (iD)

[1] Institute of Active Polymers and Berlin-Brandenburg Center for Regenerative Therapies (BCRT), Helmholtz-Zentrum Hereon, Kantstr. 55, 14513 Teltow, Germany
[2] Institute of Chemistry, University of Potsdam, Potsdam, Germany
[3] Present Address: Institute of Pharmacy, Martin-Luther-University Halle-Wittenberg, Halle, Germany
a) Address all correspondence to these authors. e-mails: andreas.lendlein@hereon.de; christian.wischke@pharmazie.uni-halle.de

Shape-memory polymer micronetworks (MN) are micrometer-sized objects that can switch their outer shape upon external command. This study aims to scale MN sizes to the low micrometer range at very narrow size distributions. In a two-step microfluidic strategy, the specific design of coaxial class capillary devices allowed stabilizing the thread of the dispersed phase to efficiently produce precursor particles in the tip-streaming regime at rates up to ~ 170 kHz and final sizes down to 4 µm. In a subsequent melt-based microfluidic photocrosslinking of the methacrylate-functionalized oligo(ε-caprolactone) precursor material, MN could be produced without particle aggregation. A comprehensive analysis of MN properties illustrated successful crosslinking, semi-crystalline morphology, and a shape-switching functionality for all investigated MN sizes (4, 6, 9, 12, 22 µm). Such functional micronetworks tailored to and below the dimension of cells can enable future applications in technology and medicine like controlling cell interaction.

Introduction

Polymer particles with the capacity to switch their shape are both conceptually fascinating and technologically relevant, e.g., for potential biological applications, where shape-dependent cellular effects including phagocytosis might be triggered on demand [1–4]. To realize a shape-switching function by the shape-memory effect (SME), an elastic polymer network structure within each individual particle is needed, as can be obtained by crosslinking [5]. For instance, network materials can be prepared by using methacrylate-functionalized telechels. Exposing droplets, which contain such telechels, to UV irradiation can induce free-radical crosslinking of the methacrylate moieties inside the droplets [6]. To introduce the shape-switching capability, the elastic network material needs to be deformed to a temporary shape by externally applied forces. This shape can be fixed, e.g., by crystallization of polymer chains, as it is often applied for semi-crystalline polymers like poly(ε-caprolactone), PCL. Alternatively, also vitrification of amorphous domains at a glass transition may be used for shape fixation [7, 8]. The shape-switching of such programmed, free-standing materials can be induced by removing the introduced temporary netpoints, i.e.,

in case of PCL by heating above the melting temperature T_m of the crystalline domains.

To obtain micronetwork (MN) particles of defined sizes with shape-memory functionality, the matrix material first needs to be templated to microparticles (MP) before conducting the internal crosslinking to MN. Obviously, this templating step will define, e.g., the dimensions and size distribution of the MN. While particle replication in non-wetting templates was conducted in selected cases [9], batch emulsification techniques have been mostly employed [6, 10–13]. Besides the distinct advantages of both of these methods to prepare micronetworks, they inherit the trade-off between replication accuracy and efficiency as reflected by accessible size distributions and sufficient production quantities. As broad size distributions may diminish the suitability of MN for explorative use in technology and medicine, such as for the use as valves or carrier systems or for mechanistic cell interaction studies with size-dependent uptake pattern in the range of 10 µm and below [14, 15], a preparation methodology would be of interest that allows both tailoring of sizes and providing very homogeneous particle populations. Furthermore,

this technique should produce relevant quantities of MN in a reproducible manner without particle aggregation such as during the crosslinking step.

Droplet-based microfluidics in devices constructed, e.g., from polydimethylsiloxane (PDMS) or glass capillaries allow preparing monodisperse droplets at specific flow settings [16–18]. It should be noted that it is often difficult to directly obtain small droplets < 20 μm under controlled conditions with this technique. Furthermore, the frequency of droplet production in the well-controlled dripping regime in single-channel devices is typically low, which has led to various attempts to increase the throughput such as by parallelization or increased per-channel productivity [19, 20]. Increasing the production rates by applying higher overall flow rates finds its boundaries in the dripping-to-jetting transition, which results in broad size distributions and occurs when either the Weber number We_i of the inner phase (i) or the capillary number Ca_o of the outer phase (o) or their sum exceed a critical value such as in the range of unity [21, 22]. This general limitation is even more pronounced for the formation of small droplets, where the volumetric flow rate ratio R_V of the outer and inner phases (correlating to their velocities u at the orifice) has to be large [23]. Accordingly, fast and precise formation of small particle in the dripping regime is, beyond issues of high-precision vibration-free pumps, conceptually limited by u_o and Ca_o.

$$We_i = \rho_i \, d_{jet} u_i^2 / \gamma, \qquad (1)$$

$$Ca_o = \eta_o u_o / \gamma, \qquad (2)$$

$$R_{\dot{V}} = \dot{V}_o / \dot{V}_i, \qquad (3)$$

with density ρ, jet diameter d_{jet}, interfacial tension γ, viscosity η, flow rate $\dot{V}$, fluid velocity u, and subscript indices i and o corresponding to the inner and outer phases, respectively.

Still, under specific conditions, particles with size distributions that are narrow compared to traditional high-shear emulsification methods can be obtained outside the dripping regime [16, 21, 23]. Of particular interest is the so-called tip-streaming mode that is characterized by a high $\dot{V}_o$ and a sharp cone (rather than a long thread) of the disperse phase formed at the orifice, from which a fine jet expands and breaks up into droplets smaller than the orifice diameter [24–26].

The goal of this study was to explore the size control of MN with shape-switching function down to a few micrometers at, importantly, narrow size distributions and sufficient throughput by the use of microfluidic preparation techniques. While microfluidic templating combined with online crosslinking is occasionally conducted for microgels from water-soluble polymers [18], here the strategy was to apply a two-step procedure. This should involve (i) a fast and stable microfluidic templating process based on organic solutions of

linear oligo(ε-caprolactone), oCL precursors bearing 2-iso-cyanatoethylmethacrylate (IEMA) end groups to create, after solvent extraction, defined MP of adjustable average diameter, and (ii) a melt-based crosslinking to convert MP to MN by network formation in the molten state, which is known to result in faster crosslinking and higher crosslinking densities compared to network formation in polymer solutions [27]. This second process should also prevent the aggregation of molten polymer droplets during crosslinking compared to bulk irradiation, as droplets will be continuously separated during transportation in a laminar flow in a microchannel. The physicochemical properties of the MN relevant for the SME should be comprehensively analyzed for the different particle sizes and their shape-switching function should eventually be demonstrated.

Results

Templating precursor particles by fast tip-streaming microfluidics

The realization of a tip-streaming condition typically requires a delicate balance of device geometry and flow conditions. This state has particularly been achieved when the liquid thread of the dispersed phase is enveloped and compressed from all sites, i.e., in rotational symmetry, by the continuous phase [28]. Considering this frame condition as well as the solvent incompatibility of PDMS devices [29], focused-flow setups built from two coaxially aligned glass capillaries were here explored first.

This setup with one outer feeding capillary and one inner collection capillary can be operated with opposing flow directions of the inner and outer fluids, which in principle enables a squeezing of the inner dispersed phase i by the outer phase o at a relatively large contact area of the fluids in front of the orifice. When such devices were run with an organic oCL-IEMA solution (8 kDa, 4.5 wt%) as i-phase and aqueous polyvinyl alcohol (PVA) solution (2.5 wt%) as o-phase, a long rather than a sharp cone was observed under tip-streaming conditions with this device geometry. Both the cone and the emitted small jet of the i-phase were instable and did not allow a continuous preparation of small particles (not shown). Furthermore, the organic phase was in contact with an adhesive-based joint of the assembly and caused its slow, but certain breakage by leaching and plastification.

By alteration of the microfluidic device, i.e., introducing a second inner needle (Fig. 1), the i-phase could be fed in close proximity and well centered in front of the collection capillary. The aqueous o-phase was provided from two inlet ports, therefore adding up the volumetric flow rates ($\dot{V}_o = \dot{V}_{o1} + \dot{V}_{o2}$ with $\dot{V}_{o1} = \dot{V}_{o2}$). In this way, a steeper cone was formed and the interfacial area between the i- and o-phases could be reduced, which substantially improved emulsification performance by avoiding

fluctuations of the cone. Specific details of the orifice distances and diameters of the feeding (O_f) and collection (O_c) capillary used in the different modes are provided in Table 1. It should be noted that depending on the desired particle sizes, this type of devices could either be operated in the dripping or the tip-streaming mode (Fig. 1).

It should be noted that the solvent selected to prepare the oCL-IEMA precursor solutions substantially affected the

production success. Preliminary experiments (not shown) revealed that oCL-IEMA solutions in dichloromethane (DCM; $\gamma_{DCM-water} = 28.3$ mN m^{-1} [30]) prevented the formation of fine jets and resulted in uncontrolled spitting, possibly due to insufficient shear-stress (small Ca_o due to large γ). In contrast, using ethyl acetate (EA) as solvent for oCL-IEMA resulted in a late formation of larger droplets further downstream. This may be justified by the influence of γ ($\gamma_{EA-water} = 6.8$ mN m^{-1} [30])
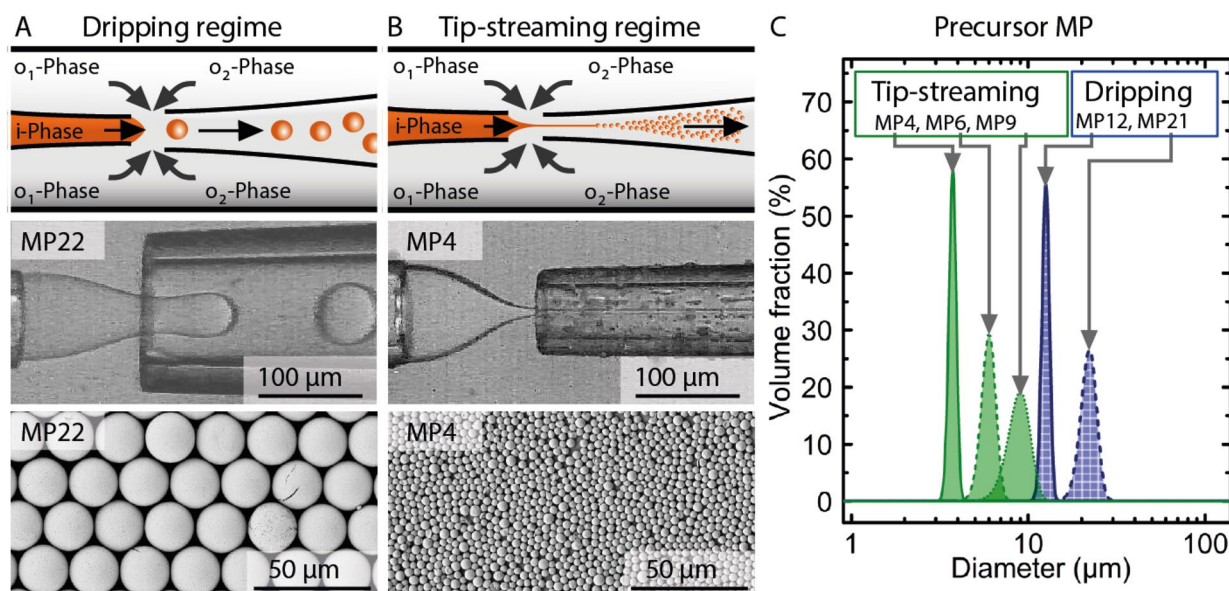
Figure 1: Microfluidic templating of oCL-IEMA MP with narrow size distribution and tailored particle sizes by emulsification of precursor solution in coaxial glass capillary microfluidics with a double-needle setup. (A and B) Schemes of setup, light microscopy images of emulsification, and SEM images of isolated MP after solvent evaporation and freeze drying for (A) dripping and (B) tip-streaming regimes. (C) Particle size distribution of precursor MP suspended in water as obtained by static light scattering (Gaussian fit of main peak, scattering artifacts removed as confirmed by SEM).

TABLE 1: Experimental parameters and results of microfluidic emulsification to template precursor MP.

Sample code	Mode[a]	Microfluidic device geometry[b]			Flow rates[c]			Droplet production characteristics[d]			Precursor MP sizes[e]	
		O_f (µm)	Dist (µm)	O_c (µm)	$\dot{V}_i$ (µL·h^{-1})	$\dot{V}_o$ (µL·h^{-1})	$R_{\dot{V}}$	d_{drop} (µm)	f_{drop} (kHz)	$\dot{m}_{oCL}$ (mg h^{-1})	$d_{MP,aq}$ (µm)	U
MP22	Drip	60	120	110	1040	8400	8.1	62	2.3	55	22.2	0.09
MP12	Drip	60	120	110	475	12,600	27	35	5.9	25	12.5	0.02
MP9	Tip-stream	75	130	55	840	24,000	29	25	28	44	9.0	0.12
MP6	Tip-stream	75	130	55	475	19,800	42	17	55	25	5.9	0.07
MP4	Tip-stream	75	130	55	360	24,000	67	10	170	19	3.7	0.00

[a]Mode of microfluidic operation: drip = dripping, tip-stream = tip-streaming.

[b]O_f = orifice diameter of inner feeding capillary (for phase i). Dist = distance between opposing inner capillaries. O_c = orifice diameter of collection capillary.

[c]Volumetric flow rate of inner phase $\dot{V}_i$ and the outer phase $\dot{V}_o$ ($\dot{V}_o = \dot{V}_{o1} + \dot{V}_{o2}$ with $\dot{V}_{o1} = \dot{V}_{o2}$). $R_{\dot{V}}$ = flow ratio [$\dot{V}_o/\dot{V}_i$].

[d]$d_{drop} = (6V_{drop}\pi^{-1})^{1/3}$; droplet diameter estimated from $d_{MP,aq}$. f_{drop} = Droplet formation frequency calculated from d_{drop} and $\dot{V}_i$. $\dot{m}_{oCL}$ = mass throughput of oCL-IEMA as calculated from $\dot{V}_i$, the polymer volume fraction of the oCL-IEMA solution and ρ_{oCL} (for details see Supplementary Information).

[e]$d_{MP,aq}$ = Volume-moment mean diameter $D[4, 3]$ and U = uniformity index (measure of absolute deviation from median) as determined by laser diffraction in water for precursor MP after solvent extraction/evaporation and freeze-drying.

on the critical thread length ($L_c \propto \eta_i/\gamma$ [31]), at which droplet formation occurs, or on the time needed for droplet pinch-off $t_{pinch} \propto d_{jet}\eta_o/\gamma$ [32]. Importantly, for a solvent mixture of EA/DCM (1:1 v/v), a stable dispersion regime was enabled. With increasing R_V, the droplet sizes were reduced and droplet formation frequencies f_{drop} increased up to very high values of 170 kHz (Table 1).

It should be highlighted that the devices could be operated under these condition in a very stable process without supervision or interference, e.g., for ~ 1 day, obtaining a mass throughput $\dot{m}_{PCL}$ of very small particles close to the gram scale in a single channel (Table 1). After solvent evaporation in a collection beaker, precursor microparticles (MP) of 4, 6, 9 μm (all tip-streaming), 12 μm, and 22 μm (both dripping regime) could be isolated. The sample codes (MP4, MP6, etc.) refer to the volume–moment mean diameter in water ($d_{MP,aq}$) as analyzed by laser diffraction in aqueous dispersion. The anticipated narrow size distributions were confirmed by both low values for uniformity U from laser diffraction analysis as well as the images collected by scanning electron microscopy (SEM) (Table 1; Fig. 1). More specifically, the size distributions of MN4 and MN6 prepared here by microfluidics ($U \leq 0.07$) were much smaller than for PCL-based 4.5 μm MN particles templated in previous work by bulk emulsification ($U = 0.5$) [6].

Micronetwork synthesis by microfluidic melt-based crosslinking

Since a polymer network structure is an essential requirement to enable shape-switching by the shape-memory effect, a covalently crosslinked structure should be synthesized by photo-induced reaction of oCL-IEMA endgroups within each individual particle. For an efficient MN formation, a suitable precursor chain mobility as given in the molten state is required to avoid network inhomogeneity. Therefore, a second microfluidic setup consisting of three different zones was constructed to enable melt-based crosslinking (Fig. 2). In a non-turbulent stream of aqueous suspension medium that apparently well separated the individual particles, the semi-crystalline precursor MP were first transported into a heating zone 1 for melting the MP at 80 °C. Subsequently, the molten precursor particles, i.e., droplets, were exposed in zone 2 to UV light (308 nm) for MN synthesis (80 °C, quartz glass capillaries with square-shaped cross section to reduce light scattering). Then, the formed MN entered a cooling zone 3 ($T < T_c$, Supplementary Table 1) to be transformed from a rubbery state to a solidified semi-crystalline morphology.

As it was a particular goal to produce MN particles of controllable and very homogeneous sizes, the prevention of aggregation and fusion during the melt-based crosslinking step should be evaluated. The size analysis of MN by laser diffraction
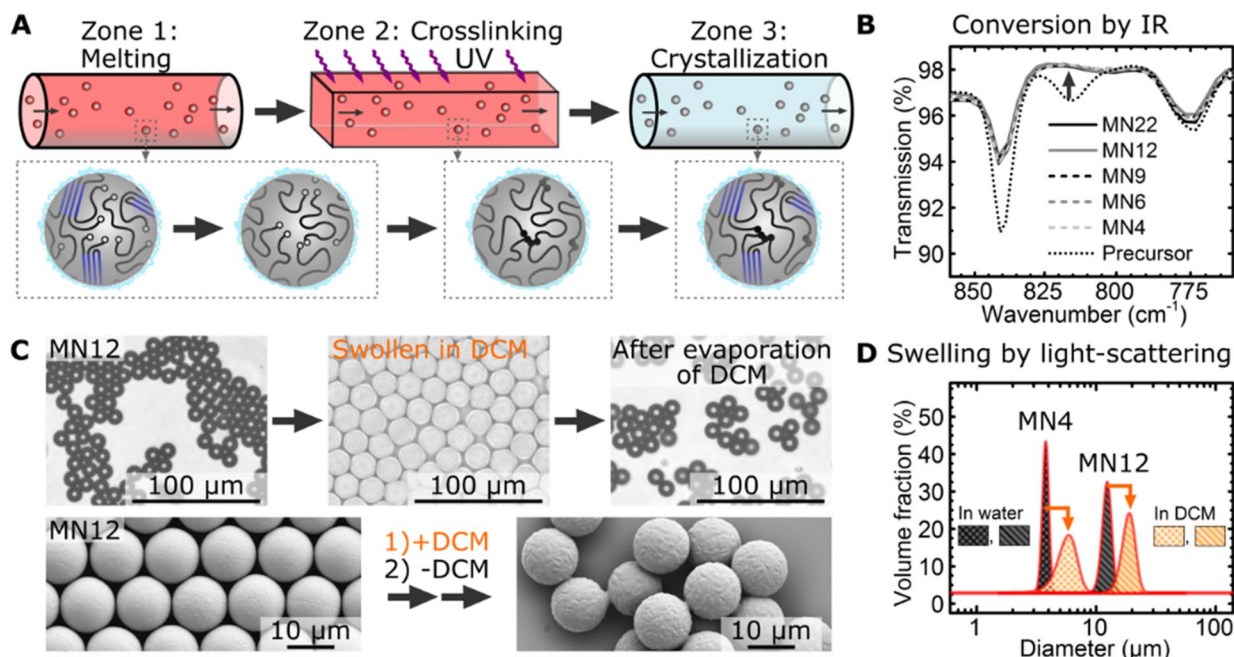
Figure 2: Microfluidic synthesis of MN from precursor MP and evaluation of micronetwork structures. (A) Schematic representation of microfluidic setup and particle transition from semi-crystalline precursor MP to molten droplets, to crosslinked MN, and eventually to semi-crystalline MN. (B) IR spectroscopy analysis of methacrylate (815 cm^{-1};=CH$_2$ out of plane vibration) conversion by crosslinking. (C) Exemplary light microscopy (top) and SEM images (bottom) of MN before, during, and after evaluation, which illustrate successful network formation by swelling studies in dichloromethane (DCM). (D) Exemplary plots of narrow size distributions of MN particles dispersed in water as well as corresponding size distribution in DCM swollen state.

(Table 2, $d_{MN,aq}$) showed excellent agreement with the sizes of the corresponding precursor MP (Table 1). Furthermore, high reproducibility was observed when several aliquots of a MP master batch were independently subjected to photocrosslinking (e.g., $d_{MN,aq}$ of master batch MP22: 22.2 μm; mean of three independent synthesis of MN22: 22.3 ± 0.1 μm). This confirms that the microfluidic setup for crosslinking provided MN without particle aggregation, i.e., the initially tailored particle sizes were preserved.

Another key goal was the formation of a covalent network structure, which should be examined by several independent techniques. FTIR spectroscopy conducted with MN powder, i.e., a large quantity of particles, allowed evaluating the conversion of methacrylate endgroups. A complete loss of the signal at 815 cm^{-1} corresponding to $=CH_2$ out-of-plane vibrations of free methacrylates clearly indicated a successful chemical reaction (Fig. 2B). Conceptually, the methacrylate's conversion into covalent netpoints of a network architecture should also result in MN swellability in a good solvent instead of dissolution, as detectable in swelling experiments. When exposing MN to DCM in a qualitative microscopic assessment on the level of individual particles, their volume substantial increased without dissolution. Importantly, the MN also readapted their initial shape after DCM evaporation (Fig. 2C; Supplementary Fig. 1). Compared to previous studies with massive gluing, bridging, or spreading of particles in case of insufficient crosslinking [6], this finding indicates that MN exhibit internal structures with entropy-elastic forces as well as a high gel content, i.e., a low portion of extractable, non-reacted oCL chains. SEM analysis confirmed no relevant volume alteration due to extracted materials (e.g., $d_{MN,SEM}$ of MN12: 12.0 ± 0.3 μm before swelling; 12.1 ± 0.3 μm after swelling) and did fit well to the results of light microscopic and laser diffraction analysis (Table 3), even though

some surface texturing was visible for all DCM-treated MN (see Fig. 2C). In order to allow a quantitative determination of the degree of swelling Q_{MN}, laser diffraction studies in DCM with larger sample aliquots were conducted (Fig. 2D). The Q_{MN} of the different MN sizes were between 265 and 575 vol% (Table 2), corresponding to an average of 380 ± 120 vol% that is in the same range as for macroscopic samples reported before (410 ± 10 vol% [33]). When adapting the Flory–Rehner theory for ideal networks (assumed netpoint functionality is 4) as a rough estimate, an average segment chain length between netpoints $M_{c,MN}$ in the range of 290 Da to 1390 Da can be calculated. Compared to the molecular weight of the oCL-IEMA precursors (8 kDa), the low M_c may be explained by physical netpoints due to chain entanglements and higher netpoint functionality. Overall, this set of analysis indicated a successful formation of a covalent network structure.

PCL has the ability to form crystallites if the polymer chains possess a suitable length and mobility for parallel orientation. The presence of PCL crystallites is indispensable for realizing a thermally induced shape-switching function of MN at conditions above ambient temperature. In case of a missing formation of PCL crystallites, only its amorphous domains may hypothetically be used for shape switching at about—60 °C, which practically may not be relevant for most applications. The thermal analysis and wide-angle X-ray scattering (WAXS) confirmed a semi-crystalline morphology of MN with melting temperatures $T_{m,MN}$ of 45–48 °C and degrees of crystallinity DOC of ~ 28% (Table 2), which are suggesting the ability of the MN to create temporary netpoints (crystallites) for temporary shape fixation as should be subsequently evaluated. A decrease in DOC, which was observed before for semi-crystalline shape-memory particles from a multiblock copolymer upon particle size reduction to

TABLE 2: Properties of MN obtained by photocrosslinking of precursor MP.

Sample code	Swelling experiments monitored by LD[a]			Analysis by Flory–Rehner model[b]		Thermal analysis by DSC[c]		Morphology by WAXS[d]	
	$d_{MN,aq}$ (μm)	$d_{MN,DCM}$ (μm)	Q_{MN} (vol%)	v_c (mmol mL^{-1})	M_c (Da)	T_m (°C)	ΔH_m (J g^{-1})	DOC (%)	l_c (nm)
MN22	22.3 ± 0.1	39.8 ± 0.1	575 ± 5	0.8 ± 0.0	1390 ± 20	45 ± 1	53.5 ± 6.0	27.5 ± 1.9	16.6 ± 0.5
MN12	12.5 ± 0.1	18.9 ± 0.0	350 ± 5	2.2 ± 0.1	520 ± 20	45 ± 1	55.9 ± 0.8	27.2 ± 3.1	16.4 ± 0.1
MN9	9.1 ± 0.0	14.1 ± 0.2	380 ± 10	1.9 ± 0.1	630 ± 40	46 ± 1	55.4 ± 1.7	28.8 ± 2.4	16.7 ± 0.7
MN6	6.1 ± 0.1	8.4 ± 0.1	265 ± 20	4.0 ± 0.8	290 ± 50	48 ± 1	56.4 ± 0.2	29.7 ± 1.0	16.9 ± 0.5
MN4	3.8 ± 0.1	5.8 ± 0.1	350 ± 5	2.2 ± 0.1	530 ± 20	48 ± 1	58.3 ± 0.8	29.4 ± 1.1	17.1 ± 0.1

[a]Volume–moment mean diameter (D[4, 3]) from particle size analysis by laser diffraction (LD) in aqueous suspension (non-swollen) and DCM (swollen) at ambient temperature; Q_{MN} = volumetric degree of swelling.

[b]Crosslink density (v_c) and average segment chain length (M_c) estimated from the swelling data by the Flory–Rehner theory (for details see Supplementary Information).

[c]T_m = melting temperature and ΔH_m = melting enthalpy from differential scanning calorimetry (DSC).

[d]DOC = degree of crystallinity and l_c = crystallite size determined by wide-angle X-ray scattering (WAXS) at ambient temperature. All results are presented as mean ± standard deviations of three independent samples.

TABLE 3: MN diameters as determined by different acquisition methods including comparison of particle sizes before ($d_{MN,aq}/d_{MN}$), during ($d_{MN,DCM}$), and after swelling ($d_{MN,after}$).

Sample code	Light microscopy			Electron microscopy		Laser diffraction			
	$d_{MN,aq}$ (μm)[a]	$d_{MN,DCM}$ (μm)[b]	$d_{MN,after}$ (μm)[c]	d_{MN} (μm)[d]	$d_{MN,after}$ (μm)[e]	$d_{MN,aq}$ (μm)[f,g] $D[4, 3]$	$d_{MN,DCM}$ (μm)[f,g] $D[4, 3]$	$d_{MN,aq}$ (μm)[f,h] $D[1,0]$	$d_{MN,DCM}$ (μm)[f,h] $D[1,0]$
MP22	22.4 ± 0.5	39.1 ± 1.1	22.5 ± 1.2	21.9 ± 0.5	21.9 ± 0.3	22.3 ± 0.1	39.8 ± 0.1	20.7 ± 0.1	39.1 ± 0.1
MP12	12.2 ± 0.4	21.0 ± 1.6	13.2 ± 0.4	12.0 ± 0.3	12.1 ± 0.3	12.5 ± 0.1	18.9 ± 0.0	12.1 ± 0.1	18.0 ± 0.0

Data display mean and standard deviation for [a]$n \geq 17$, [b]$n \geq 16$, [c]$n \geq 12$, [d]$n \geq 41$, and [e]$n \geq 42$ particles. [c,e]After swelling in DCM and subsequent solvent evaporation. [f]Mean and standard deviation from three independently crosslinking batches determined by laser diffraction. [g]$D[4, 3]$ is the volume-weighted mean diameter. [h]$D[1,0]$ is the number-weighted mean diameter calculated from $D[4, 3]$.

the submicron size range [34], motivated the determination of DOC and l_c for the MN here. These properties did not vary for the particle dimensions investigated in this study.
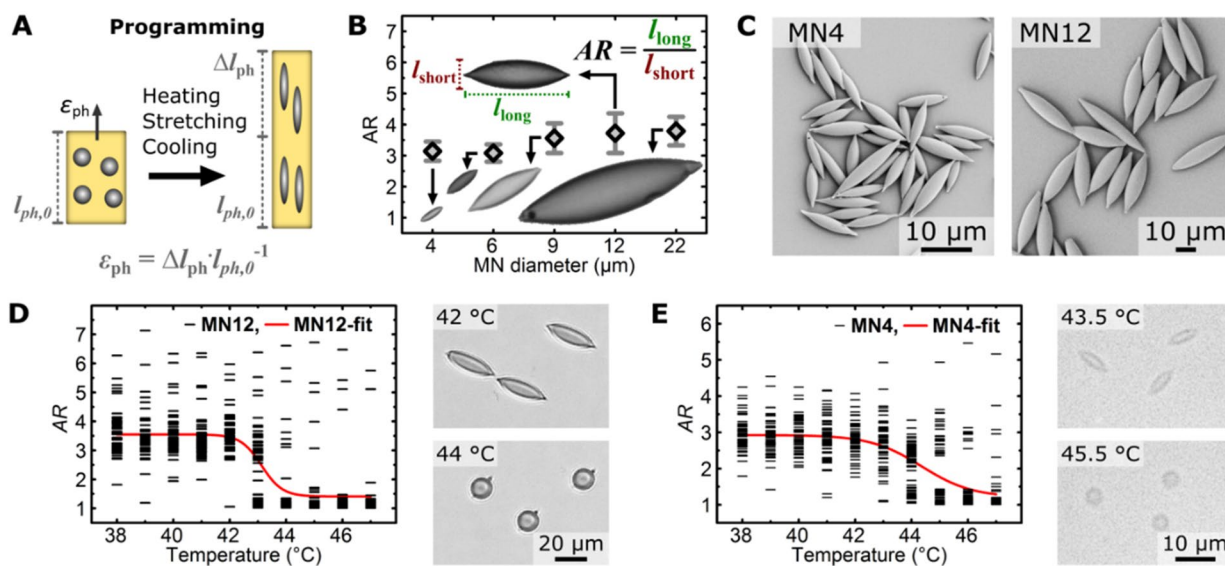
Evaluation of shape-switching function of MN

In order to prove the shape-switching functionality of size-controlled MN prepared by the microfluidic two-step process, the spherical MN should be programmed to an ellipsoidal shape by the phantom method. This process includes embedding MN particles in a phantom (polymer film) made of polyvinyl alcohol, which allows simultaneous deformation of numerous MN particles in a tensile tester. The applied phantom elongation $\varepsilon_{ph} = 175\%$ at 70 °C ($T > T_{m,MN}$) translates to an elastic deformation of incorporated MN (Fig. 3). After cooling in the elongated state to 0 °C, i.e., below the crystallization temperature of PCL domains (Supplementary Table 1), the temporary ellipsoidal

particle shape could by fixed and the programmed MN could subsequently be successfully isolated as ellipsoids by phantom dissolution.

This temporary shape can be described by the particles' aspect ratio AR (see Fig. 3B). When investigating effects of MN size on programming, an apparently slightly diminished AR was determined for smaller MN ($AR_{MN22} = 3.7 \pm 0.6$, $AR_{MN4} = 3.1 \pm 0.3$), which was mainly assigned to the resolution limits of microscopic analysis (Fig. 3B).

Upon heating in aqueous dispersion, the MN showed a shape recovery to spherical shapes (AR = 1) by fast shape switching, which is driven by entropy elasticity of the polymer network. For instance, MN12 exhibited a switching temperature T_{sw} of 43 °C, which was determined by the inflection point of the AR profile plotted over the temperature (Fig. 3D). Only a few particles (5% at $T > 43$ °C) appeared to switch at higher temperatures, which is probably due to a lower v_c as

Figure 3: Evaluation of shape-switching functionality of MN. (A) Scheme of programming by phantom elongation. (B) Impact of MN size on AR ($\varepsilon_{ph} = 175 \pm 1\%$) as analyzed by automated microscopy. (C) Exemplary SEM images of programmed MN particles. (D and E) Temperature-induced shape recovery of MN as monitored by the aspect ratio AR of the MN during heating experiments for MN12 (D) and MN4 (E). The black lines in the left plots represent data of individual particles and the right images show the particle shape slightly before and after reaching the switching temperature.

also indicated by their initially high AR > 4.5. For MN4, the T_{sw} was slightly increased to 44 °C and the switching temperature interval was broadened as may be explained by the increased T_m of those MN, different populations of crystalline domains in the MN, and/or other experimental parameters influenced by particle size such as sedimentation or mobility in convectional flow.

When comparing the shape-memory performance of MN particles to some miniaturized SMP matrices of 4–30 μm from multiblock copolymers that comprise only physical netpoints [34], a difference in the recovery behavior of PCL-based MN becomes obvious. Those PCL-PPDL multiblock copolymer particles showed only a partial shape recovery (e.g., 28–57% depending on particle size), when exceeding the T_m range associated to the PCL switching domains, whereas the full recovery (up to 92%) requires also the melting of PPDL crystallites, which as well contribute to the fixation of the temporary shape in these materials [34]. In contrast, in the covalently crosslinked PCL-MN, a quantitative recovery is reached when exceeding the $T_{m, PCL}$ range for all studied MN sizes.

Conclusions

Overall, this study illustrated that tip-streaming emulsification in the reported double-needle glass capillary microfluidic setup can be applied as a robust templating approach for polymeric precursor solutions into droplets < 20 μm, i.e., a size control to the low micrometer range and a fast production can be achieved. The transformation of the obtained MP from photocrosslinkable oligomers into MN was realized in a subsequent melt-based microfluidic process, which allowed preserving the particles' sizes and narrow size distributions without fusion events. This step resulted in defined MN with entropy elasticity and the capability to form crystalline domains. By successful programming and shape recovery experiments, the functionality of MN tailored to the sizes of cells could be demonstrated. It will be of high interest to explore such switchable particles, now available in suitable quantities, for applications in technology and medicine, e.g., to control cellular uptake or to act as valves in microcapillaries.

Materials and methods

Precursor synthesis and characterization

The polymer network precursor (oCL-IEMA) was synthesized by nucleophilic addition of hydroxyl endgroups of oligo(ε-caprolactone) diol [^{2}oCL, 8 kDa, Perstorp, UK] to 2-isocyanatoethylmethacrylate (IEMA) [34] (see Supplementary Information). The degree of functionalization as determined by ^{1}H-NMR ($D_{a,NMR}$) was 99% (Supplementary Fig. 2, Supplementary Eq. 1) and the number average molecular weight

M_n was 8100 g·mol^{-1} as determined by GPC (polydispersity PD 1.5; Supplementary Fig. 3). Differential scanning calorimetry (DSC; method see below) showed a T_m of 54 °C for oCL-IEMA.

Design and operation of microfluidic devices for emulsification of oCL-IEMA solutions to precursor MP

The microfluidic emulsification devices were constructed from two coaxially aligned inner micropipettes of spherical shape as prepared from capillaries [inner dimension (ID) = 0.58 mm Ø; outer dimension (OD) = 1.0 mm Ø] with a micropipette puller (P-1000, Sutter Instruments), which were fixed at a certain orifice distance in a squared outer capillary (ID = 1.1 × 1.1 mm, OD = 1.35 × 1.35 mm) by epoxy glue (all connected to a glass slide for better fixation and handling; setup see Supplementary Fig. 4). A pressure-driven pump (Elveflow OB1 Base Dual, 0–2000 mbar, ESI v2.6.1 software, Elvesys, Paris, France) and thermal flow sensors (1 × 0.12–4.8 mL h^{-1}, p_{max} = 100 bar; 2 × 1.8–60 mL h^{-1}, p_{max} = 5 bar, Elvesys) calibrated with the aid of syringe pumps (AL 1010, WPI, Supplementary Fig. 5) for the respective fluids were used to control the flow rates. Microfluidic emulsification was monitored with a high-speed light microscope (see below).

The inner phase i was composed of oCL-IEMA (625 mg, ρ_{oCL} ~ 1.16 g mL^{-1}) dissolved in a mixture of ethyl acetate (EA, ρ_{EA} = 0.894 g· mL^{-1}) and dichloromethane (DCM, ρ_{DCM} = 1.33 g mL^{-1}) [1:1 vol, 11.875 mL, $\rho_{EA,DCM}$ = 1.11 g mL^{-1}; ρ determined at 20 °C with DMA 4500, Anton Paar], i.e., having a calculated mass fraction of oCL-IEMA of w_{oCL} = 4.5 wt%. The aqueous outer phases o_1 and o_2 were both supplemented with 2.5 wt% (2.5 g in 97.5 mL) of polyvinyl alcohol (PVA, Mowiol® 4-88; 88% hydrolyzed, M_n = 12.6 kDa, polydispersity PD = 2.5). The emulsions were formed at volumetric flow rates V as indicated in Table 1. The droplets volumes as well as the droplet formation frequencies (f_{drop}) were calculated according to Supplementary Eqs. 2 and 3. Nascent particles were collected in an open bath for solvent extraction/evaporation and gently stirred (overhead stirrer, ≥ 5 h) until solidified MP were obtained. Finally, the suspensions of MP were centrifuged (3500 rpm MP9–22, 4500 rpm MP4, 50 mL screw cap vial) to increase the MP mass fractions to ~ 1 wt% (10 mg mL^{-1}) by removing aqueous phase.

Design and operation of microfluidic setup for MN synthesis by melt-based photocrosslinking

UV-induced crosslinking was performed in a microfluidic setup (Figs. 2, 4) comprising three modules (details see below) with

a total channel length of ~ 2 m (passage time: $t_{pass} = 7.5$ min). Syringe pumps (AL 1010, WPI) provided the suspension of precursor MP (10 mg mL^{-1}, $\dot{V}_{susp}$) in 2.5 wt% aqueous PVA solution (Mowiol® 4-88) and a pure PVA solution ($\dot{V}_{PVA}$) at defined ratios summing up a total continuous flow rate of $\dot{V}_{cont} = 12.5$ mL h^{-1} through a feeding channel (ID = 1.0 mm Ø, OD = 1.6 mm Ø, FEP tubing [fluorinated ethylene propylene, ProLiquid]) to the microfluidic device. To exclude oxygen-based side reaction during the crosslinking, both solutions were pre-treated by three freeze–pump–thaw cycles (argon) to remove dissolved oxygen before loading into syringes, which were sealed until use. After flooding the system with the PVA solution, the process started in interval I_1 of 52 min with flow rates of $\dot{V}_{susp,1} = 11.5$ mL h^{-1} and $\dot{V}_{PVA,1} = 1.0$ mL h^{-1}, while flow rates of $\dot{V}_{susp,2} = 0$ mL h^{-1} and $\dot{V}_{PVA,2} = 12.5$ mL h^{-1} were applied in interval I_2 for 25 min in order to achieve a quantitative harvest of the MN. Module 1: Preheating zone (30 cm, 80 °C, stirred water bath, $t_{pass} = 1.1$ min) composed of FEP tubing shielded from UV light by aluminum foil. Module 2: Heated UV-cell (1 m, $t_{pass} = 4.9$ min) built from 6 parallel assembled and serially connected squared quartz–glass capillaries (each 15 cm, ID = 1.0 × 1.0 mm, OD = 2.0 × 2.0 mm) connected by FEP tubing connectors (each 3 cm). Heating (80 °C) was performed on a metal plate, where a good heat transfer was ensured by an intermediate layer of oil. UV irradiation at 308 nm was provided by a XeCl-Excimer (Bluelight® Curing module BLC 308/600 50 Hz, Heraeus, distance of 4 cm, 95% output, intensity of 92 mW cm^{-2}). Module 3: FEP tubing immersed in a cooling bath (40 cm, 0 °C, $t_{pass} = 1.5$ min).

For purification, the collected semi-crystalline MN was washed on a 0.45 µm filter (Whatman®, NL 17) with pure water until a lack of bubble formation indicated removal of all excess PVA. Finally, MN were transferred into a tube, frozen in liquid nitrogen, and lyophilized (Alpha 1-2LD plus, Christ).

Particle characterization

Images of particles were collected by scanning electron microscopy (Gemini Supra™ 40 VP, Carl Zeiss NTS, with Ir-coating), light microscopy (DMI 6000B, Leica, swelling studies in DCM), high-speed light microscopy (VW 6000E, Keyence, droplet templating), and automated light microscopy (Morphology G3, Malvern Instruments, shape analysis). Volume-weighted size distributions were determined by laser diffraction [in water or DCM (Supplementary Eqs. 4, 5 and 6); Mastersizer 2000, Malvern] and shown as $D[4, 3]$ (volume–moment mean diameter), excluding scattering artifacts as confirmed by SEM. Dried MN powders were studied by ATR FTIR spectroscopy (Nicolet 6700, Thermo Scientific), DSC (DSC 204 F1, Netzsch; in nitrogen atmosphere, – 100 to 150 °C, 10 K min^{-1}), and WAXS (D8 Discover X-ray diffractometer, Bruker). A more detailed description is available in the Supporting Information.

Evaluation of shape-switching function of MN

Programming of MN was performed after embedding in PVA phantoms [10]. Briefly, 7.5 mg MP suspended in 1.5 mL of 23 wt% PVA (Mowiol® 3-85) was surrounded by pure PVA solution and dried, followed by deformation in a tensile tester (ZP 20, Zwick) to phantom elongations $\varepsilon_{ph} = 175\%$ (30 mm min^{-1}) at 70 °C and cooling to 0 °C at 10 K min^{-1}. By phantom dissolution in water, programmed ellipsoidal MN were obtained as aqueous suspension.

The shape-switching function was studied microscopically upon heating aqueous suspensions of programmed MN (10 K min^{-1}; LTS 350 stage chamber, Lincam) on a microscope slide, which was covered with a thin glass cover slide, with video recording (Axio Imager.A1m, Carl Zeiss Microimaging).
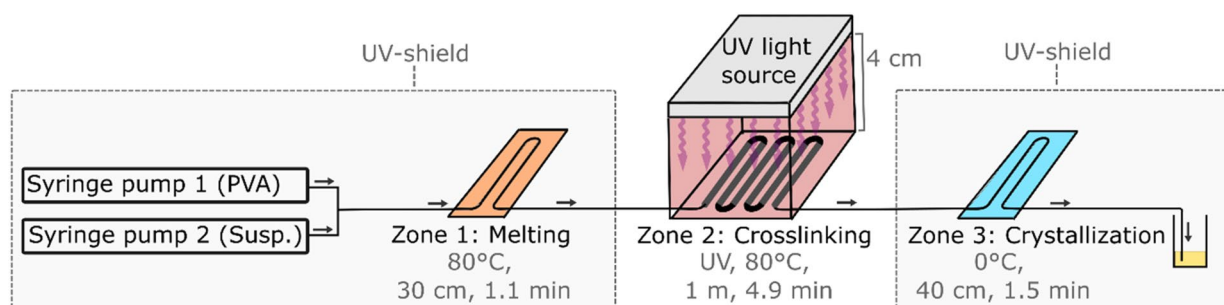
Figure 4: Microfluidic setup for UV-induced MN synthesis in melt. The setup is connected to two syringe pumps: (1) supplies pure PVA solution and (2) supplies precursor MP suspended in PVA solution. Both supply channels are combined in a T-junction. The injected material passes a preheating zone, the UV zone, and a cooling zone. Finally, MN suspensions are collected.

Acknowledgements

Funding

Data availability

The datasets generated and/or analyzed during this study are stored for an appropriate time frame at the institution, where the work has been conducted, and can be made available on reasonable request.

Declarations

Conflict of interest The authors have no commercial or any other conflict of interest in publishing this work. This work has been authorized for publication.

Open Access

Supplementary Information

The online version contains supplementary material available at https://doi.org/10.1557/s43578-021-00295-2.

References

1. N. Doshi, S. Mitragotri, Macrophages recognize size and shape of their targets. PLoS ONE **5**(4), e10051 (2010)
2. J.C. Sunshine, K. Perica, J.P. Schneck, J.J. Green, Particle shape dependence of CD8$^+$ T cell activation by artificial antigen presenting cells. Biomaterials **35**(1), 269 (2014)
3. R. Mathaes, G. Winter, A. Besheer, J. Engert, Influence of particle geometry and PEGylation on phagocytosis of particulate carriers. Int. J. Pharm. **465**(1–2), 159 (2014)
4. N. Doshi, B. Prabhakarpandian, A. Rea-Ramsey, K. Pant, S. Sundaram, S. Mitragotri, Flow and adhesion of drug carriers in blood vessels depend on their shape: a study using model synthetic microvascular networks. J. Control. Release **146**(2), 196 (2010)
5. K. Wei, G.M. Zhu, Y.S. Tang, T.T. Liu, J.Q. Xie, The effects of crosslink density on thermo-mechanical properties of shape-memory hydro-epoxy resin. J. Mater. Res. **28**(20), 2903 (2013)
6. F. Friess, U. Nochel, A. Lendlein, C. Wischke, Polymer micronetworks with shape-memory as future platform to explore shape-dependent biological effects. Adv. Healthc. Mater. **3**(12), 1986 (2014)
7. L.M. Cox, J.P. Killgore, Z. Li, R. Long, A.W. Sanders, J. Xiao, Y. Ding, Influences of substrate adhesion and particle size on the shape memory effect of polystyrene particles. Langmuir **32**(15), 3691 (2016)
8. J. Huang, L. Lai, H. Chen, S. Chen, J. Gao, Development of a new shape-memory polymer in the form of microspheres. Mater. Lett. **225**, 24 (2018)
9. S.M. Brosnan, A.-M.S. Jackson, Y. Wang, V.S. Ashby, Shape memory particles capable of controlled geometric and chemical asymmetry made from aliphatic polyesters. Macromol. Rapid Commun. **35**(19), 1653 (2014)
10. C. Wischke, A. Lendlein, Method for preparation, programming, and characterization of miniaturized particulate shape-memory polymer matrices. Langmuir **30**(10), 2820 (2014)
11. Q.Y. Guo, C.J. Bishop, R.A. Meyer, D.R. Wilson, L. Olasov, D.E. Schlesinger, P.T. Mather, J.B. Spicer, J.H. Elisseeff, J.J. Green, Entanglement-based thermoplastic shape memory polymeric particles with photothermal actuation for biomedical applications. ACS Appl. Mater. Interfaces **10**(16), 13333 (2018)
12. Y.K. Bai, J.W. Zhang, J.P. Ju, J.M. Liu, X. Chen, Shape memory microparticles with permanent shape reconfiguration ability and near infrared light responsiveness. React. Funct. Polym. **157**, 104770 (2020)
13. F.H. Zhang, T.H. Zhao, D. Ruiz-Molina, Y.J. Liu, C. Roscini, J.S. Leng, S.K. Smoukov, Shape memory polyurethane microcapsules with active deformation. ACS Appl. Mater. Interfaces **12**(41), 47059 (2020)
14. M.P. Desai, V. Labhasetwar, E. Walter, R.J. Levy, G.L. Amidon, The mechanism of uptake of biodegradable microparticles in Caco-2 cells is size dependent. Pharm. Res. **14**(11), 1568 (1997)
15. P. Pacheco, D. White, T. Sulchek, Effects of microparticle size and fc density on macrophage phagocytosis. PLoS ONE **8**(4), e60989 (2013)
16. Z. Nie, M. Seo, S. Xu, P. Lewis, M. Mok, E. Kumacheva, G. Whitesides, P. Garstecki, H. Stone, Emulsification in a

microfluidic flow-focusing device: effect of the viscosities of the liquids. Microfluid. Nanofluid. **5**(5), 585 (2008)

17. R.K. Shah, H.C. Shum, A.C. Rowat, D. Lee, J.J. Agresti, A.S. Utada, L.-Y. Chu, J.-W. Kim, A. Fernandez-Nieves, C.J. Martinez, D.A. Weitz, Designer emulsions using microfluidics. Mater. Today **11**(4), 18 (2008)

18. M. Hua, Y. Du, J. Song, M. Sun, X. He, Surfactant-free fabrication of pNIPAAm microgels in microfluidic devices. J. Mater. Res. **34**(1), 206 (2019)

19. T. Nisisako, T. Torii, Microfluidic large-scale integration on a chip for mass production of monodisperse droplets and particles. Lab. Chip **8**(2), 287 (2008)

20. C. Wischke, Concepts for efficient preparation of particulate polymer carrier systems by droplet -based microfluidics. Int. J. Pharm. **584**, 119401 (2020)

21. A.S. Utada, A. Fernandez-Nieves, H.A. Stone, D.A. Weitz, Dripping to jetting transitions in coflowing liquid streams. Phys. Rev. Lett. **99**(9), 094502 (2007)

22. N.M. Kovalchuk, M. Sagisaka, K. Steponavicius, D. Vigolo, M.J.H. Simmons, Drop formation in microfluidic cross-junction: jetting to dripping to jetting transition. Microfluid. Nanofluid. **23**(8), 103 (2019)

23. G.T. Vladisavljević, W.J. Duncanson, H.C. Shum, D.A. Weitz, Emulsion templating of poly(lactic acid) particles: droplet formation behavior. Langmuir **28**(36), 12948 (2012)

24. W.-C. Jeong, J.-M. Lim, J.-H. Choi, J.-H. Kim, Y.-J. Lee, S.-H. Kim, G. Lee, J.-D. Kim, G.-R. Yi, S.-M. Yang, Controlled generation of submicron emulsion droplets via highly stable tip-streaming mode in microfluidic devices. Lab. Chip **12**(8), 1446 (2012)

25. R. Suryo, O.A. Basaran, Tip streaming from a liquid drop forming from a tube in a co-flowing outer fluid. Phys. Fluids **18**(8), 082102 (2006)

26. J.M. Montanero, A.M. Ganan-Calvo, Dripping, jetting and tip streaming. Rep. Prog. Phys. **83**(9), 097001 (2020)

27. F. Friess, A. Lendlein, C. Wischke, Photoinduced synthesis of polyester networks from methacrylate functionalized precursors: analysis of side reactions. Polym. Adv. Technol. **25**(11), 1285 (2014)

28. X. Xu, R. Song, M. He, C. Peng, M. Yu, Y. Hou, H. Qiu, R. Zou, S. Yao, Microfluidic production of nanoscale perfluorocarbon droplets as liquid contrast agents for ultrasound imaging. Lab. Chip **17**(20), 3504 (2017)

29. A.R. Abate, D. Lee, T. Do, C. Holtze, D.A. Weitz, Glass coating for PDMS microfluidic channels by sol–gel methods. Lab. Chip **8**(4), 516 (2008)

30. W. Apostoluk, J. Drzymała, An improved estimation of water–organic liquid interfacial tension based on linear solvation energy relationship approach. J. Colloid Interface Sci. **262**(2), 483 (2003)

31. T. Cubaud, T.G. Mason, Capillary threads and viscous droplets in square microchannels. Phys. Fluids **20**(5), 053302 (2008)

32. A.S. Utada, E. Lorenceau, D.R. Link, P.D. Kaplan, H.A. Stone, D.A. Weitz, Monodisperse double emulsions generated from a microcapillary device. Science **308**(5721), 537 (2005)

33. F. Friess, C. Wischke, M. Behl, A. Lendlein, Oligo(epsilon-caprolactone)-based polymer networks prepared by photo-crosslinking in solution. J. Appl. Biomater. Funct. Mater. **10**(3), 273 (2012)

34. M. Balk, M. Behl, U. Nochel, A. Lendlein, Shape-memory hydrogels with switching segments based on oligo(omega-pentadeca-lactone). Macromol. Mater. Eng. **297**(12), 1184 (2012)